

Determination of the anti-glioblastoma effect of artesunate and its potential targets through RNA-seq data analysis

zijing ren (✉ renzijing8@126.com)

Xiangyang No 1 People's Hospital Affiliated to Hubei University of Medicine

qiang zhao

Xiangyang No 1 People's Hospital Affiliated to Hubei University of Medicine

Jing Tian

Xiangyang No 1 People's Hospital Affiliated to Hubei University of Medicine

Xingyue li

Hubei University of Medicine

yue wang

Hubei University of Medicine

ming Sang

Hubei University of Medicine

peiyang Zhou

Xiangyang No 1 People's Hospital Affiliated to Hubei University of Medicine

Research Article

Keywords: Artesunate, glioblastoma, proliferation, protein-protein interaction network, RNA sequencing, reactive oxygen species

Posted Date: April 22nd, 2022

DOI: <https://doi.org/10.21203/rs.3.rs-1563193/v1>

License: © ⓘ This work is licensed under a Creative Commons Attribution 4.0 International License.

[Read Full License](#)

Abstract

Background: Glioblastoma (GBM) is an invasive brain tumor that lacks effective treatment methods. This study examined the effects and molecular mechanisms of Artesunate (ART) in GBM using both *in vivo* and *in vitro* methods and RNA sequencing (RNA-seq).

Methods and Results: The effects of ART were assessed *in vitro* using GBM cells and *in vivo* using tumor-bearing nude mice. ART significantly suppressed GBM cell proliferation, facilitated apoptosis, and induced excessive reactive oxygen species (ROS) generation. However, ROS scavengers reversed the growth inhibitory and apoptotic effects of ART on GBM cells. In the mouse model of GBM, ART effectively inhibited cancer development without inducing toxicity. RNA-seq of ART-treated and untreated cells revealed 389 differentially expressed genes (DEGs), including 145 upregulated and 244 downregulated DEGs. Furthermore, the DEGs were applied to Gene Ontology and Kyoto Encyclopedia of Gene and Genomes analysis. The downregulated DEGs were mostly related to tumor-related pathways, such as the cell cycle, cell molecule adhesion, and extracellular matrix-receptor interaction. In addition, analyses using the Molecular Complex Detection algorithm and protein-protein interaction network were performed on those DEGs, and HMMR, CDC20, CCNB1, and THBS1, which may play key roles in ART-treated GBM cells, were identified. These results were validated via quantitative PCR and western blot analysis.

Conclusions: Overall, our results illustrated the anti-GBM effects of ART and the possible mechanisms involved.

1 Introduction

Glioblastoma (GBM) is a frequently occurring primary brain cancer with high aggressiveness and a very poor prognosis. Generally, GBM is treated by surgical resection combined with chemoradiotherapy; however, the median survival of patients is as low as 15 months [1, 2]. Therefore, it is necessary to examine potential anti-GBM drugs to improve therapeutic outcomes. The major obstacle to GBM treatment is that most experimental drugs cannot cross the blood-brain barrier (BBB) to achieve effective treatment.

Artesunate (ART), an esterified derivative of antimalarial artemisinin, can cross the BBB [3]. Compared with artemisinin, ART has a high solubility and bioavailability and is more widely used. The hydrophobicity of ART allows easy penetration into the cell membrane to exert an anti-tumor effect. ART has shown profound toxicity to tumor cells *in vivo*, *in vitro*, and in clinical studies [4–9]. The inhibitory effect of ART on GBM has been suggested in some studies, and the related molecular mechanisms include downregulation of survivin gene expression [10], induction of oxidative breaks in double-stranded DNA (dsDNA) [11], inhibition of homologous recombination [12], enhancement of chemotherapeutic effects of temozolomide [13], and promotion of radiosensitization [2]. However, clinical studies have shown that ART may induce organ damage, especially liver toxicity [14], indicating the need for further studies on the efficacy and mechanism of ART against GBM.

RNA sequencing (RNA-seq) uses deep sequencing technology to provide precise information about transcriptional profiles. This offers significant advantages for the analysis of drug treatment effects, including the identification of drug-related differentially expressed genes (DEGs). Additionally, protein-protein interaction (PPI) network and functional enrichment analyses are helpful in understanding the molecular mechanisms of drug action. Although ART has been suggested to suppress GBM growth, the underlying gene regulatory mechanism remains unclear.

The present study focused on examining the effect of ART on GBM suppression and the related mechanisms using *in vivo* and *in vitro* experiments and RNA-seq analysis. The findings of this study could improve our understanding of the anti-GBM effect of ART and help in identifying target genes and pathways for effective GBM treatment.

2 Materials And Methods

2.1 Cell Culture

Human GBM U87 and U251 cells were obtained from their cell bank of Chinese Academy of Sciences (Shanghai, China), and cultivated them within using Dulbecco's modified Eagle's medium (Gibco, China), containing 1% penicillin-streptomycin and 100 mL/L fetal bovine serum (Absin, China), at 5% CO₂ and 37°C.

2.2 Cell Viability Assay

The CCK8 kit (Biosharp, China) was used for determining cell viability. In brief, we plated U87 and U251 cells ($4 \times 10^3/100 \mu\text{L}/\text{well}$) into 96- well plates and cultured them overnight. Thereafter, cell treatment and incubation were conducted for a 2-h period in a medium containing 10 μL CCK8 under 37°C. Finally, the scanning multi-well spectrophotometer (Molecular Devices, USA) was utilized to measure the absorbance (OD) value at 450 nm.

2.3 Apoptosis Analysis

The Annexin V-FITC Apoptosis Kit (BD Biosciences, USA) was used for analyzing cell apoptosis. Briefly, we cultured U251 and U87 cells ($4 \times 10^5/2 \text{ mL}/\text{well}$) and collected them using a 0.25% trypsin solution without EDTA after treatment with varying concentrations of ART (final concentration of 0, 12.5, 25, and 50 μM) for 48 h. After rinsing twice with phosphate-buffered saline (PBS), the cells were subjected to a 0.5 h incubation with the Annexin-V-FITC staining solution in the dark under ambient temperature. Then, the cells were further stained for a 5 min period with 5 μL propidium iodide (PI), prior to analysis using the FACSCalibur flow cytometer (FCM; BD, USA) to measure apoptosis.

2.4 Western blotting (WB)

The RIPA lysis buffer (Beyotime, China) containing the protease inhibitor cocktail (Beyotime) was utilized for cell or tumor tissue lysis on ice, followed by total protein isolation. We later adopted the BCA protein

concentration assay kit (Beyotime) for determining protein content. After separation of aliquots of proteins via sodium dodecyl-sulfate polyacrylamide gel electrophoresis, they were transfer onto a polyvinylidene fluoride membrane (Millipore, USA). The membrane was then incubated with the antibodies against caspase3 and cleaved-caspase3 (1:1000; Cell Signaling Technology, USA); Bcl2 (1:1000; Absin); Bax (1:1000; Absin); HMMR (1:1000; Proteintech, China); CDC20 (1:1000; Wanleibio, China); CCNB1 (1:1000; Wanleibio); THBS1 (1:1000; Elabscience, China); and β -actin (1:2000; Absin) at 4°C. After washing with TBST, the membrane was further incubated with an anti-mouse or anti-rabbit secondary antibody (1:2000) under ambient temperature for 1 h. Finally, the membrane was washed with TBST, and the antibodies were detected using a chemiluminescent detection system (Bio-Rad ChemiDoc, USA).

2.5 ROS Assay

Intracellular ROS were detected using the DCFH-DA assay kit (Beyotime), with fluorescence intensity proportional to intracellular ROS level. The fluorescence-labeled cells were visualized using a fluorescent microscope (Olympus, Tokyo, Japan).

2.6 Determination of Mitochondrial Membrane Potential (MMP, $\Delta\psi_m$)

A mitochondrial membrane potential assay kit (KeyGEN, China) was adopted for measuring the MMP of ART-treated U87 and U251 cells. Briefly, we inoculated U251 and U87 (5×10^4 /mL/well) into 12-well plates and incubated overnight. Afterward, the original medium was discarded, and the medium containing ART (final concentration of 0, 12.5, 25, and 50 μ M) was added and incubated for 48 h. Three replicate wells were created for each concentration gradient. After washing with PBS, the cells were treated with the JC-1 staining solution (400 μ L) and incubated for 20 min in the dark. Finally, the MMP was determined using FCM.

2.7 Mito-Tracker Red CMXRos Staining

After the indicated treatments, Mito-Tracker Red CMXRos dye and 4', 6-diamidino-2-phenylindole (DAPI) (both Beyotime) were used for cell staining. In brief, at the end of the intervention, the medium was aspirated and the cells were incubated in Mito-Tracker Red CMXRos (200 nM final concentration) at 37°C for 20 min. After washing twice with PBS, DAPI was added and the cells were incubated for another 10 min, followed by observation under a fluorescence microscope.

2.8 Mice Tumor Models

Briefly, 4×10^6 U87 cells were suspended in PBS (100 μ L), and the cell suspension was administered to male BALB/C-nu mice via the right armpit (4-week-old; Hunan SJA Laboratory Animal Co., Ltd, China). At seven days post-injection, all animals were randomly assigned to ART (100 mg/kg, n = 8) or DMSO (control, n = 6) groups. Changes in body weight and tumor volume were recorded. The tumor volume was calculated as follows: $V = 0.52 \times L \times W^2$, (V = volume, L = length, W = width). Eventually, the organs and

tumors of mice were isolated for histological analysis (hematoxylin-eosin staining, HE) and immunohistochemistry (IHC).

2.9 IHC

The tumor tissue was embedded in paraffin, sliced into 5 μm -thick slices, and placed onto the slides. After deparaffinization using xylene, each section was subjected to gradient ethanol rehydration. Antigen retrieval was performed by immersing the slides in an antigen repair buffer for 10 min in a 95°C water bath. Following this, each section was cooled to ambient temperature and incubated in 3% H_2O_2 for 15 min to remove peroxidase activity. Thereafter, the sections were blocked with the goat serum under ambient temperature for 30 min. The samples were then incubated with an anti-Ki67 primary antibody (Proteintech) overnight at 4°C. This was followed by a 1 h incubation with an HRP-labeled secondary antibody (Proteintech) under ambient temperature. Finally, 3, 3'-diaminobenzidine-tetrahydrochloride-dihydrate (Solarbio, China) was added to visualize the sections using an optical microscope.

2.10 Terminal-deoxynucleotidyl Transferase Mediated Nick-end Labeling (TUNEL)

The TUNEL apoptosis detection kit (Beyotime) was used to detect the apoptosis of cancer cells according to specific protocols. A fluorescence microscope was employed to examine the stained cells.

2.11 mRNA-Seq, Data Preprocessing, and Enrichment Analysis

After 48 h of ART treatment (50 μM), U251 cells were rinsed twice with PBS. Then, Trizol was added to store the RNA, and the sample was sent to the Nanjing Tongyuan Medical Laboratory for construction of RNA-Seq libraries, quantification, and paired-end sequencing using Illumina NovaSeq 6000. hisat2 [15] was used to align the reads against the human reference genome (hg38) with default parameters. The gene read count matrix was extracted using the featureCounts [16] method. We used DESeq2 [17] to detect the significant DEGs with a threshold value of $|\log_2 \text{fold change (FC)}| > 1$ and Benjamini-Hochberg corrected $p < 0.05$. Thereafter, Gene Ontology (GO) as well as Kyoto Encyclopedia of Gene and Genomes (KEGG) databases were adopted for the over representation enrichment analysis of the downregulated and upregulated gene sets in clusterProfiler [18]. All analyses were conducted using the R 4.0.2 platform.

2.12 PPI Network Construction and Module Analysis

Based on the STRING database (<http://STRING-db.org>), this study established a PPI network on the basis of DEGs with default parameters. The Cytoscape software (version 3.9.0) was employed for visualizing the PPI network. Later, the densely connected proteins from the PPI topological networks were identified using the Molecular Complex Detection (MCODE) algorithm (<https://apps.cytoscape.org/apps/mcode>) with default parameters. The protein clusters with the highest cluster score were selected for further verification.

2.13 Quantitative PCR (qPCR) Analysis

After ART treatment, RNA was extracted from U251 cells using the Trizol reagent according to the standard RNA isolation procedure. Then, the PrimeScript™ IV 1st strand cDNA Synthesis Mix (Takara, China) was utilized to synthesize the cDNA through reverse transcription, and qPCR amplification was performed with TB Green® Fast qPCR Mix (Takara) using the following primers: HMMR, 5'-TCCAGGTGCTTATGATGT-3' (Forward, F); 5'-GAAGCAGGCAAGGTAGTA-3' (Reverse, R); CDC20, 5'-GAAGACCTGCCGTTACAT-3' (F); 5'-TTCCCAGAACTCCAATCC-3' (R); CCNB1, 5'-GCACTTTCCTCCTTCTCA-3' (F); 5'-CGATGTGGCATACTTGTT-3' (R); THBS1, 5'-CAGCAGCCGCTTTTATGT-3' (F); 5'-GTGGTGGAGTTTACAACCTTCA-3' (R).

2.14 Statistical Analysis

GraphPad Prism 8 was employed for data analysis using an unpaired Student's *t*-test. Results are presented as the mean ± SD of values from three assays. A one-way analysis of variance was utilized to determine differences across different groups. *P* < 0.05 was considered statistically significant.

3 Results

3.1 ART Inhibited GBM Cell Proliferation and Promoted GBM Cell Apoptosis

To determine the effect of ART on GBM cell proliferation *in vitro*, U251 and U87 cells were treated with varying concentrations of ART, for different durations, and examined using the CCK8 assay. We found that ART time- and dose-dependently inhibited the growth of GBM cells. U251 cells showed enhanced ART sensitivity compared to U87 cells (Fig. 1a and b).

To estimate the role of ART in GBM cell apoptosis, U87 and U251 cells were treated with ART (0, 12.5, 25, and 50 μM) for 48 h, and apoptosis was determined via FCM. ART was found to induce U251 and U87 cell apoptosis dose-dependently (Fig. 1c and d). Furthermore, relative to those in the control, the Bax/Bcl2 and cleaved caspase3/caspase3 ratios were upregulated in ART-treated U251 and U87 cells, as revealed by WB (Fig. 1e and f).

3.2 ART Induced ROS Secretion and Mitochondrial Destruction in Human GBM Cells

The main anti-tumor or anti-malarial mechanism of ART is the formation of ROS via the cleavage of an endoperoxide bridge [3, 19, 20]. Consistent with earlier research, we found that ART increased intracellular ROS levels dose-dependently, as detected using DCFH-DA (Fig. 2a and b). High ROS levels have been implicated in mitochondrial destruction. Therefore, we examined the Δψ_m of the cells using the specific mitochondrial probe JC-1. ART treatment reduced the MMP of U87 and U251 cells (Fig. 2c and d).

However, a cell proliferation assay showed that N-Acetyl-L-cysteine (NAC) reversed ART toxicity in U251 and U87 cells (Fig. 3a). Furthermore, the results of Mito-Tracker Red CMXRos staining revealed that ART treatment resulted in a reduction in the number of bioactive mitochondria, and NAC treatment inhibited

the ART-induced decrease in fluorescence signal intensity (Fig. 3b), which indicated that NAC may scavenge ART-induced ROS, thereby reducing mitochondrial damage. Moreover, pretreatment with NAC partially reversed the ART-induced changes in Bax, Bcl2, and cleaved-caspase3 expression (Fig. 3c and d). Overall, ART exposure caused mitochondrial destruction and suppressed cell proliferation while inducing apoptosis, by enhancing ROS accumulation in GBM cell lines.

3.3 ART Significantly Inhibited Tumor Growth in Tumor-bearing Mice

To examine the anti-tumor effect of ART on GBM *in vivo*, each GBM model mouse was administered 100 mg/kg/day ART on day 7 after modeling, and tumor growth was analyzed. Tumors were excised on day 28. Although no significant difference was observed in mouse body weight (BW) (Fig. 4a), the ART-treated group had decreased tumor size, weight, and volume compared with the control group (Fig. 4b–d). Additionally, IHC analysis showed that ART treatment resulted in reduced Ki67 expression (Fig. 4e). TUNEL staining revealed that ART treatment promoted GBM cell apoptosis (Fig. 4f). The change in the trends of the expression of apoptosis-related proteins Bcl2 and Bax in the tumor tissue was consistent with the intracellular results (Fig. 4g and h). Additionally, the ART-treated mice did not exhibit signs of toxicity or inflammatory lesions (Fig. 4i).

3.4 Transcriptome Analysis of ART-treated U251 Cells

To explore the potential molecular mechanism of ART against GBM cells, we used RNA-seq to investigate the transcriptome level changes in U251 cells exposed 50 μ M ART for 48 h. A total of 389 DEGs, including 145 upregulated and 244 downregulated genes in the ART-treated samples, were identified via DEG analysis in the treated group compared with the those in the control group (Fig. 5a).

Furthermore, the downregulated DEGs within the ART-induced U251 cells were most significantly enriched in positive regulation of developmental processes in BP, intermediate filament in CC, and modified amino acid binding in MF, as revealed by GO analysis (Fig. 5b, Supplemental Table 1). Additionally, the upregulated DEGs showed significant enrichment in MF terms, such as acting on paired donors, incorporation of one atom each of oxygen into both donors, oxidoreductase activity, 2-oxoglutarate as one donor, and with incorporation/reduction of molecular oxygen (Supplemental Table 2). Furthermore, KEGG enrichment analysis revealed that the downregulated DEGs showed major enrichment in cell adhesion molecules (CAMs), cell cycle markers, and ECM-receptor interactions (Fig. 5c, Supplemental Table 3), while the upregulated DEGs were not enriched in any pathway. We found that the downregulated gene enrichment KEGG pathway results were related to tumor progression and migration. Overall, these results indicated the potential mechanisms of the anti-GBM effects of ART.

3.5 PPI Enrichment Analysis and Verification

We then performed PPI network enrichment analysis and verification of the upregulated and downregulated DEGs. In order to detect the most important ART anti-tumor proteins, we used the MCODE

algorithm to detect the highly interconnected protein clusters within the PPI network constructed in the present study. As a result, the downregulated PPI network had three clusters with scores of 24.74, 5.4, and 4.5 (Fig. 5d–f), while the maximum cluster score of the upregulated network was 3 (Supplementary Fig. 1). According to the KEGG enrichment results, the cluster 1 and cluster 2 proteins were related to cancer-associated pathways, such as the ECM-receptor interaction and cell cycle. We believe that the downregulated cluster proteins involved in these pathways play an important role in the ART-induced anti-GBM mechanism. Next, we chose four genes, CDC20, CCNB1, HMMR in cluster 1 and THBS1 in cluster 2, for further gene and protein level validation (Fig. 5g–k). The result shows that tendency of the protein levels were similar to those of the RNA. We believe that these genes may drive the GBM anti-tumor effects of ART.

4 Discussion

GBM is a frequently occurring nervous system cancer, characterized by high aggressiveness and poor response to radiotherapy and chemotherapy. GBM is a serious threat to human health, with no effective treatment options. However, the development of naturally-derived substances as novel chemopreventative medicines is promising in GBM research. Artemisinin, ART, and other derivatives exhibit extensive biological activities, such as antitumor and antioxidation activity [21]. However, studies have yet to comprehensively examine the effects and underlying mechanism of ART in human GBM.

In this study, ART suppressed the proliferation of U87 and U251 cells depending on time and its dose. When the concentration increased, ART treatment elevated cell apoptotic rates, reduced Bcl2 (an anti-apoptotic protein) level, and upregulated the expression of pro-apoptotic protein Bax and cleaved-caspase3. The major anti-tumor mechanism of ART may be related to endoperoxide bridge cleavage, causing ROS production [19, 20, 22]. We found that ART also promoted ROS accumulation in U251 and U87 cells. Generally, the mitochondrion is the major site for intracellular ROS production, but high levels of ROS can induce intracellular damage, especially mitochondrial disruption [23].

The $\Delta\psi_m$ is an important parameter of mitochondrial activity and function. Our results suggested that ART exposure reduced the MMP of both U251 and U87 cells. ART may induce mitochondrial damage by increasing ROS levels. Use of an ROS scavenging reagent and Mito-Tracker confirmed that ART could reduce the Mito-Tracker labeling intensity of U251 cells; however, NAC reversed this phenomenon. CCK8 and WB assays further confirmed that NAC could reverse the effect of ART on cell activity as well as apoptosis-related or anti-apoptotic-related protein levels. Efferth *et al.* reported that antioxidants or transfection of antioxidant genes can attenuate ART-induced tumor cell death [24], which was consistent with our findings.

The subcutaneous tumor-bearing technique was used to visually detect the growth of tumors in nude mice. There was a delay in tumor development and decreased Ki67 expression in ART-treated mice relative to controls. TUNEL staining and WB further confirmed that ART treatment exploited the anti-GBM effect. Currently, the safety of ART in antitumor applications has received increasing attention. The

results of histological analysis of organs from tumor-bearing nude mice showed that ART intervention did not cause any obvious visceral damage.

Furthermore, transcriptomic analysis of ART-treated U251 cells identified 389 DEGs, including 244 downregulated and 145 upregulated genes. KEGG pathway enrichment analysis showed that ART mainly inhibited ECM-receptor interaction, CAMs, and cell cycle regulation in U251 cells. This study utilized the STRING database to establish a PPI network based on the identified DEGs, followed by module analysis using Cytoscape. We identified CDC20, CCNB1, HMMR, and THBS1 as potential driver proteins of the anti-glioma effect of ART. Among these proteins, CDC20 and CCNB1 were mainly involved in cell cycle regulation. HMMR is a novel hyaluronan receptor that regulates cell motility and is highly expressed in GBM tumors [25, 26]. HMMR is less expressed in normal tissues, and its overexpression can lead to centrosome and mitotic abnormalities [27, 28]. Thus, HMMR is a possible target to treat GBM [25]. THBS1 is a matricellular protein that contributes to the invasive behavior of GBM [29]. THBS1 levels can predict the survival rate of GBM patients [30]. To verify the RNA-seq results, we also detected the mRNA and protein levels of CDC20, CCNB1, HMMR, and THBS1 in U251 cells. qPCR and WB analyses showed that ART significantly downregulated these genes at the RNA and protein levels. We believe that these could serve as potential targets for the treatment of GBM, or the secondary consequences of DNA damage caused by ART-induced ROS. However, this needs to be further verified using recovery experiments.

5 Conclusion

In summary, ART suppressed GBM growth *in vivo* and *in vitro*. Additionally, based on the RNA-seq analysis, we identified four key genes, *HMMR*, *CDC20*, *CCNB1*, and *THBS1*, which may be potential therapeutic targets against GBM. Our findings provide valuable information for better elucidating the anti-GBM effects and molecular mechanisms of ART.

Declarations

Funding

This work was supported by grants from the Scientific and Technological Project of Xiangyang City of Hubei Province (2020YL20) and Innovative Research Program of Xiangyang No.1 People's Hospital.

Competing Interests

The authors have no relevant financial or non-financial interests to disclose.

Author Contributions

Peiyang Zhou, Zijing Ren, and Ming Sang designed the experiments. Zijing Ren, Xingyue Li, and Yue Wang performed the majority of the experiments and analyzed the data. Ming Sang was involved in the investigation and supervision. Zijing Ren and Qiang Zhao wrote the manuscript and formatted figures.

Jing Tian helped to revise the manuscript. Zijing Ren and Peiyang Zhou obtained the funding. All authors read and approved the final manuscript.

Acknowledgments

We thank Xiaodong Sun for her technical support and Lixia Xie for her help with the mouse-related experiments.

Data Availability

All data are provided in the article and supplementary information. All other data supporting the findings of this study are available upon request from the corresponding authors.

Ethics Approval

This study was reviewed and approved by the Animal Welfare and Research Ethics Committee of Xiangyang NO. 1 People's Hospital (2019DW007).

References

1. Martínez-García M, Álvarez-Linera J, Carrato C, Ley L, Luque R, Maldonado X, Martínez-Aguillo M, Navarro LM, Vaz-Salgado MA, Gil-Gil M (2018) SEOM clinical guidelines for diagnosis and treatment of glioblastoma (2017). *Clin Transl Oncol* 20:22–28. <https://doi.org/10.1007/s12094-017-1763-6>
2. Yang LJ, Zhou CF, Lin ZX (2014) Temozolomide and radiotherapy for newly diagnosed glioblastoma multiforme: a systematic review. *Cancer Investig* 32:31–36. <https://doi.org/10.3109/07357907.2013.861474>
3. Gautam A, Ahmed T, Batra V, Paliwal J (2009) Pharmacokinetics and pharmacodynamics of endoperoxide antimalarials. *Curr Drug Metab* 10:289–306. <https://doi.org/10.2174/138920009787846323>
4. Efferth T, Dunstan H, Sauerbrey A, Miyachi H, Chitambar CR (2001) The anti-malarial artesunate is also active against cancer. *Int J Oncol* 18:767–773. <https://doi.org/10.3892/ijo.18.4.767>
5. Li X, Gu S, Sun D, Dai H, Chen H, Zhang Z (2018) The selectivity of artemisinin-based drugs on human lung normal and cancer cells. *Environ Toxicol Pharmacol* 57:86–94. <https://doi.org/10.1016/j.etap.2017.12.004>
6. Våtsveen TK, Myhre MR, Steen CB, Wälchli S, Lingjærde OC, Bai B, Dillard P, Theodossiou TA, Holien T, Sundan A, Inderberg EM, Smeland EB, Myklebust JH, Oksvold MP (2018) Artesunate shows potent anti-tumor activity in B-cell lymphoma. *J Hematol Oncol* 11:23. <https://doi.org/10.1186/s13045-018-0561-0>
7. Beccafico S, Morozzi G, Marchetti MC, Riccardi C, Sidoni A, Donato R, Sorci G (2015) Artesunate induces ROS- and p38 MAPK-mediated apoptosis and counteracts tumor growth in vivo in

- embryonal rhabdomyosarcoma cells. *Carcinogenesis* 36:1071–1083.
<https://doi.org/10.1093/carcin/bgv098>
8. Du JH, Zhang HD, Ma ZJ, Ji KM (2010) Artesunate induces oncosis-like cell death in vitro and has antitumor activity against pancreatic cancer xenografts in vivo. *Cancer Chemother Pharmacol* 65:895–902. <https://doi.org/10.1007/s00280-009-1095-5>
 9. Krishna S, Ganapathi S, Ster IC, Saeed MEM, Cowan M, Finlayson C, Kovacsevics H, Jansen H, Kreamsner PG, Efferth T, Kumar D (2015) A randomised, double blind, placebo-controlled pilot study of oral artesunate therapy for colorectal cancer. *EBioMedicine* 2:82–90.
<https://doi.org/10.1016/j.ebiom.2014.11.010>
 10. Reichert S, Reinboldt V, Hehlhans S, Efferth T, Rödel C, Rödel F (2012) A radiosensitizing effect of artesunate in glioblastoma cells is associated with a diminished expression of the inhibitor of apoptosis protein survivin. *Radiother Oncol* 103:394–401.
<https://doi.org/10.1016/j.radonc.2012.03.018>
 11. Berdelle N, Nikolova T, Quiros S, Efferth T, Kaina B (2011) Artesunate induces oxidative DNA damage, sustained DNA double-strand breaks, and the ATM/ATR damage response in cancer cells. *Mol Cancer Ther* 10:2224–2233. <https://doi.org/10.1158/1535-7163.MCT-11-0534>
 12. Berte N, Lokan S, Eich M, Kim E, Kaina B (2016) Artesunate enhances the therapeutic response of glioma cells to temozolomide by inhibition of homologous recombination and senescence. *Oncotarget* 7:67235–67250. <https://doi.org/10.18632/oncotarget.11972>
 13. Karpel-Massler G, Westhoff MA, Kast RE, Dwucet A, Nonnenmacher L, Wirtz CR, Debatin KM, Halatsch ME (2014) Artesunate enhances the antiproliferative effect of temozolomide on U87MG and A172 glioblastoma cell lines. *Anti Cancer Agents Med Chem* 14:313–318.
<https://doi.org/10.2174/18715206113136660340>
 14. Uhl M, Schwab S, Efferth T (2016) Fatal liver and bone marrow toxicity by combination treatment of dichloroacetate and artesunate in a glioblastoma multiforme patient: case report and review of the literature. *Front Oncol* 6:204. <https://doi.org/10.3389/fonc.2016.00204>
 15. Kim D, Langmead B, Salzberg SL (2015) HISAT: a fast spliced aligner with low memory requirements. *Nat Methods* 12:357–360. <https://doi.org/10.1038/nmeth.3317>
 16. Liao Y, Smyth GK, Shi W (2014) featureCounts: an efficient general purpose program for assigning sequence reads to genomic features. *Bioinformatics* 30:923–930.
<https://doi.org/10.1093/bioinformatics/btt656>
 17. Love MI, Huber W, Anders S (2014) Moderated estimation of fold change and dispersion for RNA-seq data with DESeq2. *Genome Biol* 15:550. <https://doi.org/10.1186/s13059-014-0550-8>
 18. Wu T, Hu E, Xu S, Chen M, Guo P, Dai Z, Feng T, Zhou L, Tang W, Zhan L, Fu X, Liu S, Bo X, Yu G (2021) clusterProfiler 4.0: A universal enrichment tool for interpreting omics data. *Innov (N Y)* 2:100141.
<https://doi.org/10.1016/j.xinn.2021.100141>
 19. Efferth T, Giaisi M, Merling A, Krammer PH, Li-Weber M (2007) Artesunate induces ROS-mediated apoptosis in doxorubicin-resistant T leukemia cells. *PLoS ONE* 2:e693.

<https://doi.org/10.1371/journal.pone.0000693>

20. Pang Y, Qin G, Wu L, Wang X, Chen T (2016) Artesunate induces ROS-dependent apoptosis via a Bax-mediated intrinsic pathway in Huh-7 and Hep3B cells. *Exp Cell Res* 347:251–260. <https://doi.org/10.1016/j.yexcr.2016.06.012>
21. Efferth T (2006) Molecular pharmacology and pharmacogenomics of artemisinin and its derivatives in cancer cells. *Curr Drug Targets* 7:407–421. <https://doi.org/10.2174/138945006776359412>
22. Chen Z, Kang X, Wu Y, Xiao H, Cai X, Sheng S, Wang X, Chen S (2019) A mitochondria targeting artesunate prodrug-loaded nanoparticle exerting anticancer activity via iron-mediated generation of the reactive oxygen species. *Chem Commun (Camb)* 55:4781–4784. <https://doi.org/10.1039/C9CC00531E>
23. Fan W, Shen T, Ding Q, Lv Y, Li L, Huang K, Yan L, Song S (2017) Zearalenone induces ROS-mediated mitochondrial damage in porcine IPEC-J2 cells. *J Biochem Mol Toxicol* 31:e21944. <https://doi.org/10.1002/jbt.21944>
24. Efferth T, Briehl MM, Tome ME (2003) Role of antioxidant genes for the activity of artesunate against tumor cells. *Int J Oncol* 23:1231–1235. <https://doi.org/10.3892/ijo.23.4.1231>
25. Tilghman J, Wu H, Sang Y, Shi X, Guerrero-Cazares H, Quinones-Hinojosa A, Eberhart CG, Laterra J, Ying M (2014) HMMR maintains the stemness and tumorigenicity of glioblastoma stem-like cells. *Cancer Res* 74:3168–3179. <https://doi.org/10.1158/0008-5472.CAN-13-2103>
26. Li J, Ji X, Wang H (2018) Targeting long noncoding RNA HMMR-AS1 suppresses and radiosensitizes glioblastoma. *Neoplasia* 20:456–466. <https://doi.org/10.1016/j.neo.2018.02.010>
27. Maxwell CA, Keats JJ, Belch AR, Pilarski LM, Reiman T (2005) Receptor for hyaluronan-mediated motility correlates with centrosome abnormalities in multiple myeloma and maintains mitotic integrity. *Cancer Res* 65:850–860
28. Maxwell CA, Keats JJ, Crainie M, Sun X, Yen T, Shibuya E, Hendzel M, Chan G, Pilarski LM (2003) RHAMM is a centrosomal protein that interacts with dynein and maintains spindle pole stability. *Mol Biol Cell* 14:2262–2276. <https://doi.org/10.1091/mbc.e02-07-0377>
29. Daubon T, Léon C, Clarke K et al (2019) Deciphering the complex role of thrombospondin-1 in glioblastoma development. *Nat Commun* 10:1146. <https://doi.org/10.1038/s41467-019-08480-y>
30. Qi C, Lei L, Hu J, Wang G, Liu J, Ou S (2021) Thrombospondin-1 is a prognostic biomarker and is correlated with tumor immune microenvironment in glioblastoma. *Oncol Lett* 21:22. <https://doi.org/10.3892/ol.2020.12283>

Figures

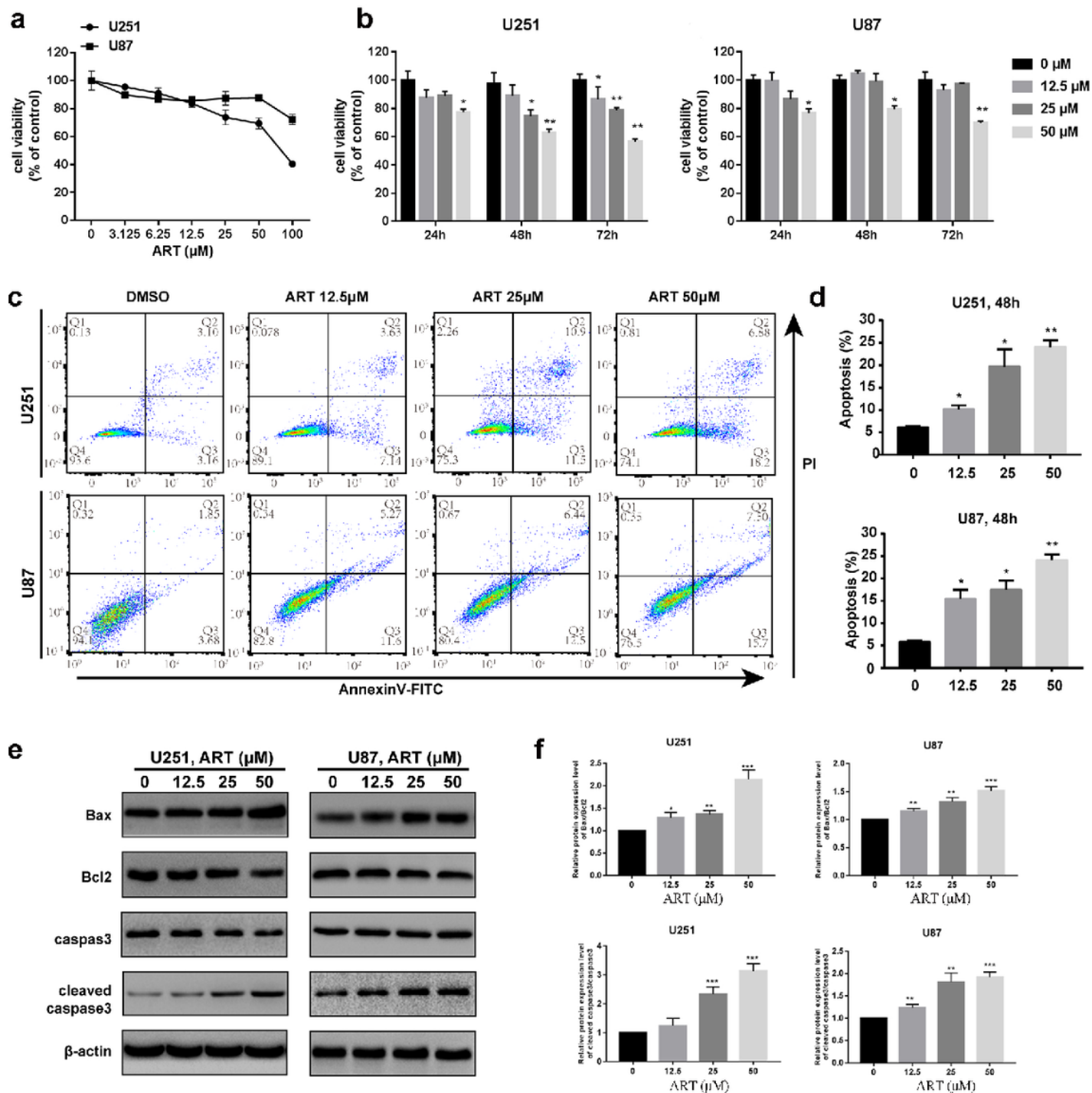


Figure 1

Artesunate (ART) inhibited U251 and U87 cellular proliferation and induced U251 and U87 cellular apoptosis

a CCK8 assay was conducted to measure U87 and U251 cell viability following a 24 h ART treatment at diverse concentrations ($n = 3$). **b** Histograms showing the viability of U251 and U87 cells subjected to 24, 48, and 72 h of ART (12.5, 25, and 50 μM) or DMSO treatment. **c–e** U251 and U87 cells were subjected to 48 h of ART (12.5, 25, and 50 μM) or DMSO treatment; each treatment was carried out thrice. **c** Flow

cytometric analysis of annexin V-FITC/PI double-stained cells. **d** The overall apoptotic cell percentage is presented as mean \pm SD. **e** Cellular proteins were collected, and the expression of cleaved caspase3, caspase3, Bcl2, and Bax was measured via western blotting. **f** The ratios of Bcl2 to Bax and cleaved caspase3 to caspase3 were calculated according to (**e**). Results are presented as mean \pm SD. * $p < 0.05$, ** $p < 0.01$, *** $p < 0.0001$ compared with control values of cells treated with DMSO alone.

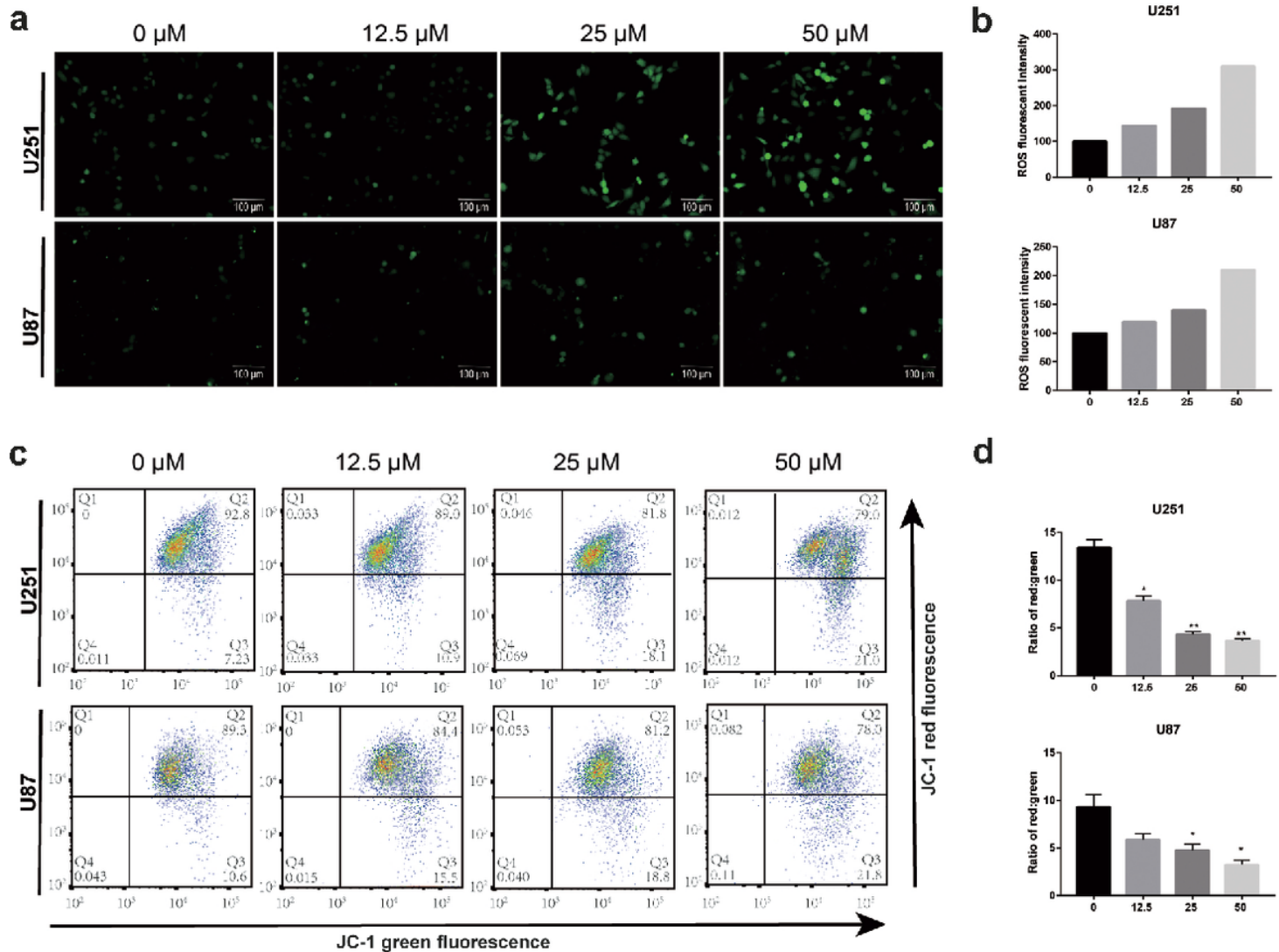


Figure 2

Artesunate (ART) induced reactive oxygen species (ROS) secretion and mitochondrial destruction in glioblastoma cells

U251 and U87 cells were subjected to 48 h of ART (12.5, 25, and 50 μ M) or DMSO treatment. **a** ROS generation was assessed via DCFH-DA staining. **b** Bar graphs represent the mean \pm SD for the ROS-positive cell fluorescence intensity from three independent experiments. **c** The altered mitochondrial membrane potential of U87 and U251 cells was analyzed using flow cytometry and JC-1 staining. **d** JC-1 red/green fluorescence ratios of diverse groups were calculated according to (**c**). * $p < 0.05$, ** $p < 0.01$ compared with control cells subject to DMSO treatment only.

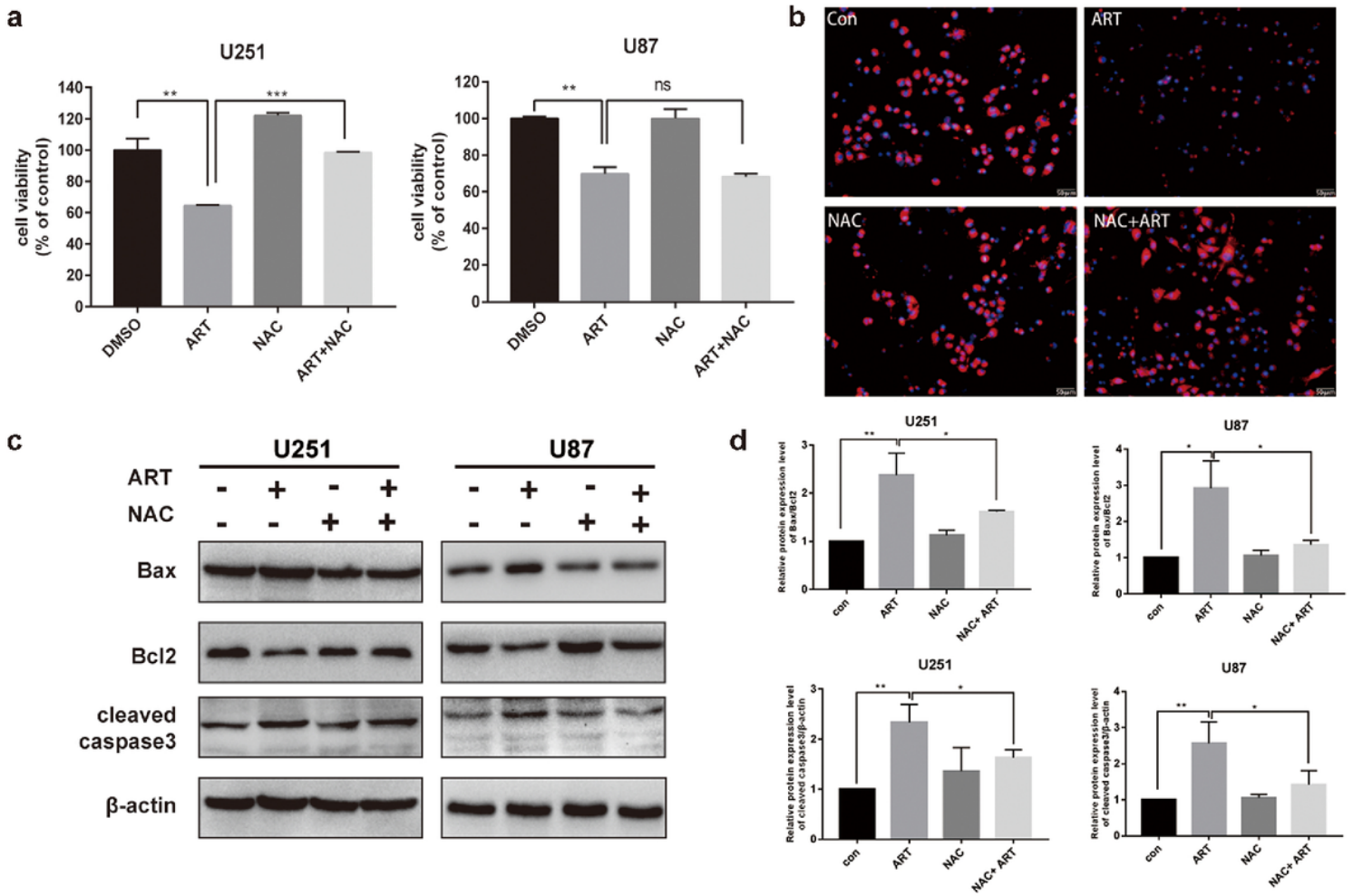


Figure 3

NAC (N-Acetyl-L-cysteine) suppressed the growth-inhibiting and pro-apoptotic effects of artesunate (ART) on glioblastoma cells

ART at 50 μ M was used to treat U87 and U251 cells for a 48 h period with or without 5 mM NAC. **a** CCK8 assay was performed for measuring cell viability. Results are presented as mean \pm SD. **b** The cells were stained with Mito-Tracker Red CMXRos, and the mitochondrial fluorescence intensity was observed using a fluorescence microscope. Blue: DAPI-stained nuclei, red: Mito-Tracker red CMXRos-stained bioactive mitochondria. **c** cleaved caspase3, caspase3, Bcl2, and Bax levels were measured using western blotting. **d** The ratios of Bcl2 to Bax and cleaved caspase3 to β -actin were calculated according to (c). Results are presented as mean \pm SD. ns, no significance, * p < 0.05, ** p < 0.01, *** p < 0.0001.

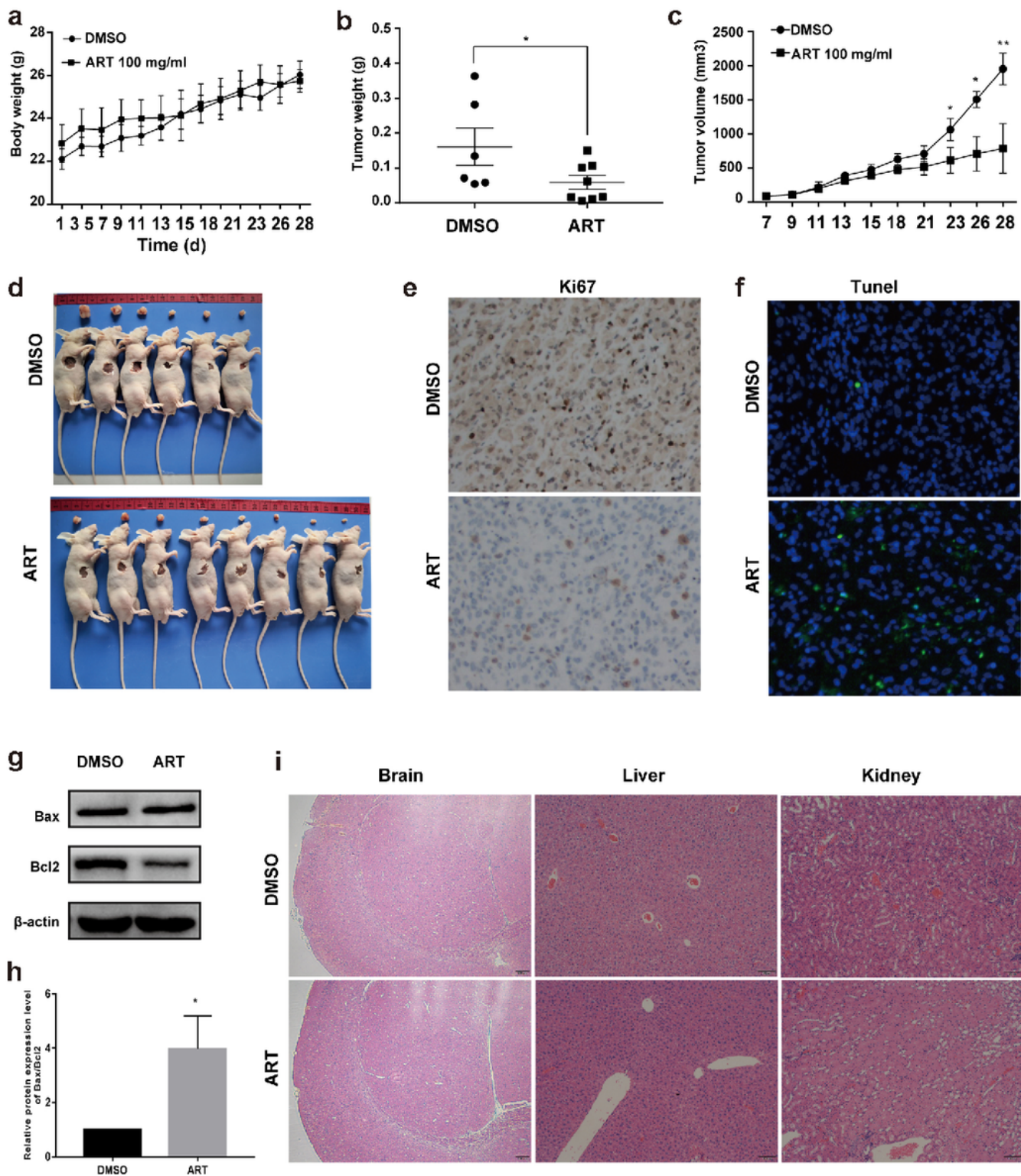


Figure 4

Artesunate (ART) significantly inhibited tumor growth in U87 tumor-bearing mice

a Body weights; **b** tumor weights; and **c** tumor volumes of tumor-bearing nude mice from ART (n = 8), and control (n = 6) groups. **d** Morphological observation of transplanted tumor from each mouse. **e** Ki67 immunohistochemical and **f** TUNEL analyses of human glioma xenograft tissue sections. **g** Levels of Bax

and Bcl2 in total protein extracts from tumor tissue were assessed via western blotting. **h** Bcl2-to-Bax ratio was determined according to **(g)**. Results are presented as mean \pm SD. **i** Hematoxylin-eosin staining of the main organs in ART-treated mice. * $p < 0.05$, ** $p < 0.01$ vs. control (DMSO).

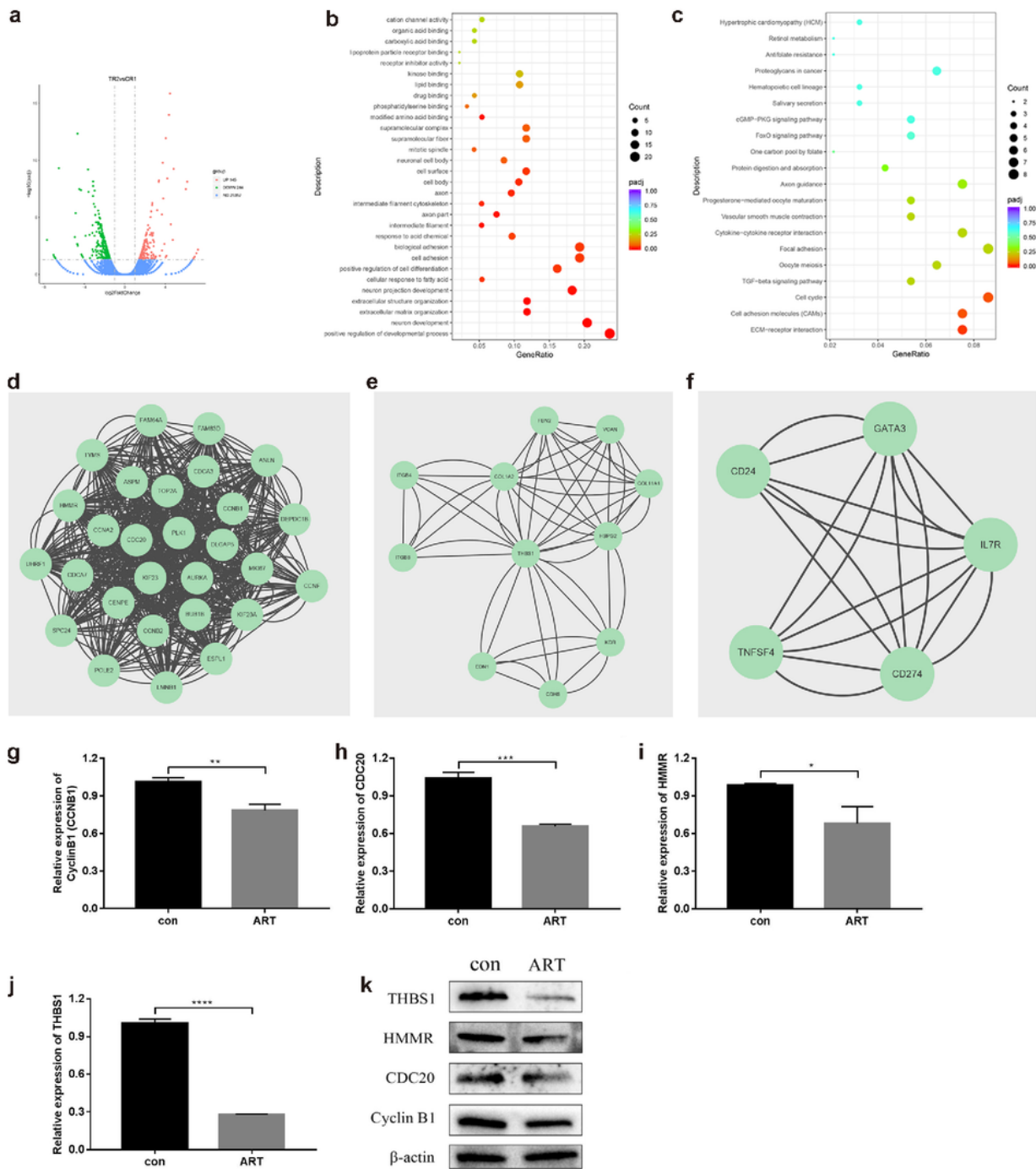


Figure 5

Transcriptome and protein-protein interaction (PPI) enrichment analyses of artesunate (ART)-treated U251 cells and verification of the expression of hub genes

a Volcano plot of genes expressed differentially (DEGs) between the two groups. **b** Dot plot showing the 20 Gene Ontology (GO) terms most significantly enriched by downregulated DEGs. **c** Dot plot of the top 20 Kyoto Encyclopedia of Gene and Genomes (KEGG) enrichment items of downregulated DEGs. Only the top three pathways showed significant enrichment. **d–f** Molecular Complex Detection PPI network and the most significant module of downregulated DEGs. The cluster scores are 24.74, 5.4, and 4.5, respectively. **g–k** Extraction of total protein and RNA from U251 cells treated with or without ART. **g–j** The expression of HMMR, CDC20, CCNB1, and THBS1 were detected by qPCR. * $p < 0.05$, ** $p < 0.01$, *** $p < 0.001$, **** $p < 0.0001$ compared with control. Results are presented as the mean \pm SD. **k** HMMR, CDC20, CCNB1, and THBS1 levels were detected by western blotting.

Supplementary Files

This is a list of supplementary files associated with this preprint. Click to download.

- [Supplementary.docx](#)
- [supplyfig.1.pdf](#)